RARE METALS

ORIGINAL ARTICLE

Sb nanoparticles encapsulated in N-doped carbon nanotubes as freestanding anodes for high-performance lithium and potassium ion batteries

Xiao-Ping Lin, Fang-Fang Xue, Zhi-Gang Zhang, Qiu-Hong Li*

Abstract Sb-based materials with high specific capacity have targeted as an alternative anode material for alkali metal ion batteries. Herein, Sb nanoparticles embedded in hollow porous N-doped carbon nanotubes (Sb@N-C nanotubes) are used as freestanding anode for Li-ion batteries (LIBs) and K-ion batteries (PIBs). The Sb@N-C nanotubes demonstrate exceptional reversible capacity of 643 mAh·g^{-1} at 0.1 A·g^{-1} with long cycle stability, as well as outstanding rate performance (219.6 mAh·g^{-1} at 10 A·g^{-1}) in LIBs. As the anode material of PIBs, they reveal impressive capacity of 325.4 mAh·g^{-1} at 0.1 A·g^{-1}. The superior electrochemical properties mainly originate from the novel structure. To be specific, the obtained 3D connected network allows for quick ion and electron migration, and prevents the aggregation of Sb nanoparticles. The hollow porous nanotubes can not only accommodate the volume expansion of Sb nanoparticles during cycling, but also facilitate the infiltration of the electrolyte and reduce the ion diffusion length. This work provides a new insight for designing advanced Sb-based anodes for alkali metal ion batteries.

Keywords Alkali metal ion batteries; Freestanding electrode; Hollow porous nanotube; Sb@N-C nanotubes

Xiao-Ping Lin and Fang-Fang Xue contributed equally to this work.

Supplementary Information The online version contains supplementary material available at https://doi.org/10.1007/s12598-022-02143-6.

X.-P. Lin, F.-F. Xue, Z.-G. Zhang, Q.-H. Li*
Pen-Tung Sah Institute of Micro-Nano Science and Technology, Xiamen University, Xiamen 361005, China
e-mail: liqiuhong@xmu.edu.cn

1 Introduction

In the past few years, with the development of new energy vehicles including intelligent mobile phone and lots of smart appliances, the market demand for high energy density and high flexibility power sources has grown rapidly [1–4]. Lithium-ion batteries (LIBs) have been widely integrated into hybrid vehicles and smart electronic equipment [5, 6]. Nevertheless, the uneven distribution of lithium resources and the high cost restrict their application in large-scale energy-related devices [7–9]. Potassium-ion batteries (PIBs) are considered as promising candidate as electrical energy storage systems because of abundant potassium resources on the earth and low redox potential (− 2.93 V (vs. standard hydrogen electrode)), close to that of lithium (− 3.04 V (vs. standard hydrogen electrode)) [10–12]. However, the large radius of K$^+$ (0.138 nm) causes sluggish diffusion kinetics and large volume expansion during repeated K-ion insertion–extraction processes [13, 14]. Although commercial graphite has been widely used in LIBs, it can no longer meet the booming demands in PIBs because of its low capacity (278 mAh·g^{-1}) [15, 16]. Therefore, it is urgent to develop suitable anode materials for LIBs and PIBs.

Antimony (Sb) has attracted much attention due to its high theoretical specific capacity (660 mAh·g^{-1}) and low reduction potential. However, the large volume expansion and pulverization of the electrode during cycling hamper its commercial application [17–20]. Lots of attempts have been made to address this issue. Dispersing nanostructured Sb into carbon matrix is one widely used method to improve the electrochemical performances of alloying materials [21, 22]. For example, Li et al. [23] reported an ultrafine Sb embedded in a porous carbon nanocomposite

(Sb@PC) through in situ substitution of the Cu nanoparticles in a metal–organic framework (MOF)-derived octahedron carbon framework, which not only provides fast transfer channels for ions and electrons but also suppresses the agglomeration and volume variation of Sb during cycling, thus ensuring the structural stability and achieving superior sodium storage performance. Furthermore, constructing hollow structure for providing substantial inner void space to tolerate large volume expansion has been demonstrated as a practicable approach to enhance electrochemical properties [24, 25]. Huang et al. [26] fabricated yolk–shell Sb@C nanoboxes embedded in carbon nanofibers (Sb@CNFs) as an enhanced anode for PIBs, in which the void space can effectively tolerate the large volume variation, and the plastic carbon shell ensures the structural stability of electrode material. Although the electrochemical performances of Sb-based anode have been improved, there still remains a big challenge to explore anodes with outstanding performances and high flexibility for alkali metal ion batteries.

Herein, we report a novel structure of Sb nanoparticles embedded in N-doped hollow carbon nanotubes (Sb@N-C nanotubes) by a typical electrospinning method followed by annealing process with polymethyl methacrylate (PMMA) as pore former. In this unique design, the 3D interconnected network can provide a fast transport way for Li/K-ions and electrons, thus accelerating reaction kinetics. Benefiting from the hollow porous structure of carbon nanotubes, the volume expansion of Sb during alloying/dealloying processes is well relieved and the infiltration of the electrolyte is enhanced. As a consequence, Sb@N-C nanotubes exhibit remarkable cycling and rate performances in LIBs and PIBs. Besides, the obtained fiber membranes exhibit high flexibility, which can be directly sliced into electrode without using binder or current collector, enhancing the energy density of Sb@N-C nanotubes electrode.

2 Experimental

2.1 Preparation of hollow Sb@N-C nanotubes

All reagents used in this work were analytical grade. Hollow Sb@N-C nanotubes were fabricated by an electrospinning method followed by high-temperature calcination. Typically, 0.912 g of $SbCl_3$, 0.5 g of polyacrylonitrile (PAN) and 0.3 g of PMMA were added into 10 ml of N, N-dimethylformamide (DMF) and then kept stirring for 24 h at room temperature to obtain a transparent precursor solution. Then, the obtained solution was transferred into a 10 ml of plastic syringe equipped with a stainless steel needle. The flow rate was kept at 0.4 ml·h^{-1} and the distance between the needle and a rolling collector was set to 15 cm. A high voltage of 15 kV was applied between the needle and collector. The obtained nanofiber mats were pre-oxidized at 230 °C for 1 h with a heating rate of 5 °C·min^{-1}, and then carbonized at 600 °C for 2 h under H_2 (5 vol%)/Ar (95 vol%) atmosphere to obtain hollow Sb@N-C nanotubes. For comparison, Sb@N-C nanofibers and pure carbon nanotubes were fabricated through the same process without adding PMMA or $SbCl_3$, respectively.

2.2 Material characterizations

The morphologies of the materials were investigated by scanning electron microscope (SEM, Zeiss SUPRA 55) and transmission electron microscope (TEM, JEOL JEM 2100). X-ray powder diffraction (XRD, Riguku Ultima IV) was carried out to observe the crystal structure of Sb@N-C nanotubes. X-ray photoelectron spectroscopy (XPS) was performed on Axis Ultra DLD Kratos AXIS SUPRA X-ray photoelectron spectra. Raman spectrum was investigated by a LabRam ARAMIS confocal micro Raman spectrometer (Horiba Jobin Yvon). Elemental analyzer (Vario EL III) was measured to observe the content of Sb, C, O and N elements.

2.3 Electrochemical measurements

The flexible Sb@N-C nanotubes films were directly cut into a round piece as freestanding electrode with a diameter of 12 mm. The weight of each piece was 1.0–1.2 mg. The electrochemical performances were conducted in CR2032 coin cells, which were fabricated in an argon-filled glove box. Lithium and potassium foils were used as the counter electrode, respectively. Celgard 2400 membranes were employed as the separators for LIBs, and Whatman glass fibers were separators for PIBs. 1.0 mol·L^{-1} LiPF$_6$ in ethylene carbonate (EC)/diethyl carbonate (DEC) and 1.0 mol·L^{-1} potassium trifluoromethanesulfonimide (KTFSI) in EC/DEC were used as the electrolyte, respectively. Cyclic voltammogram (CV) measurements were conducted on Chenhua CHI 660E with the voltage window ranging from 0.01 to 3 V (vs. Li/Li$^+$) and 0.01 to 2.5 V (vs. K/K$^+$), respectively. Electrochemical impedance spectroscopy (EIS) was tested at a frequency of 1×10^{-2} – 1×10^5 Hz.

3 Results and discussion

As illustrated in Fig. 1, the synthesis of hollow Sb@N-C nanotubes follows a typical electrospinning method and subsequently calcination process. Firstly, the solution of
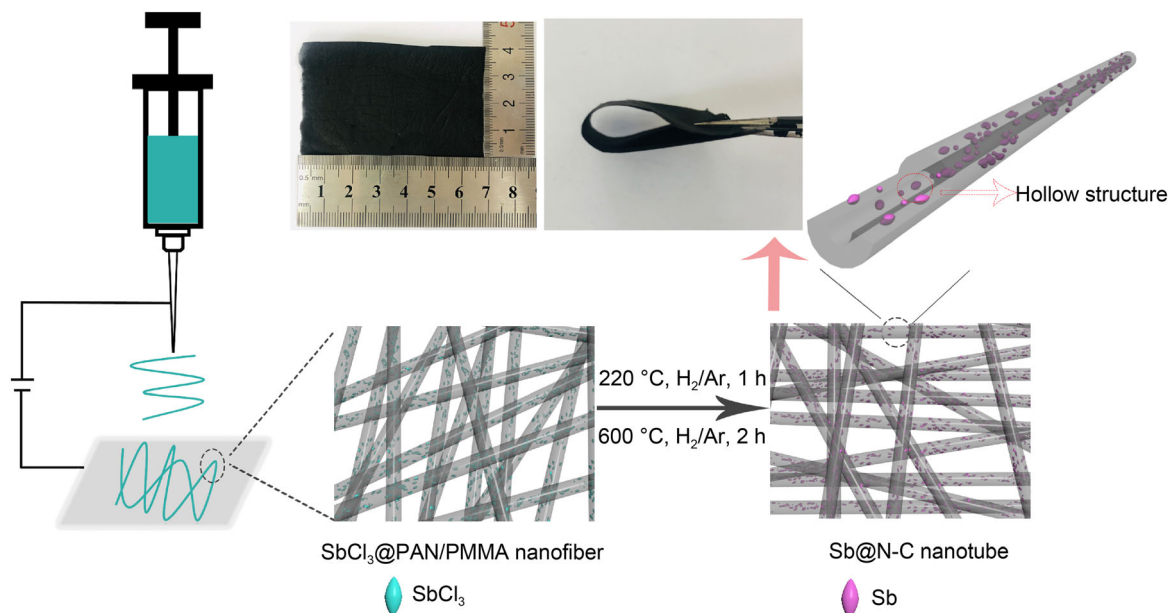
Fig. 1 Schematic illustration for preparation of hollow Sb@N-C nanotubes

SbCl$_3$, PMMA and PAN in DMF is electrospun into a precursor nanofiber. During electrospinning, a PMMA-PAN core–shell jet is formed because PAN/DMF solution is easier to stretch than a PMMA/DMF fluid [27, 28]. After pre-oxidation at 230 °C, the stabilized nanofibers are carbonized, and SbCl$_3$ are reduced to Sb nanoparticles in H$_2$/Ar atmosphere at 600 °C. During this calcination, PMMA begin to decompose at around 270 °C and degrade completely without carbon residue at approximately 400 °C, while continuous PAN phase is easily transformed into carbon, leading to the formation of hollow N-doped nanotubes [29, 30]. The obtained fiber membrane exhibits high flexibility which can be rolled up at any angle as shown in Fig. S1.

Figure 2a displays the XRD patterns of Sb@N-C nanotubes, pure carbon nanotubes and Sb@N-C nanofibers. In pure carbon nanotubes, a broad peak appearing at 25.8° is corresponding to the (002) plane of graphite. As for Sb@N-C nanotubes, the diffraction peaks located at 25.2°, 28.7°, 40.1°, 41.9° and 51.6° are indexed to the (101), (012), (104), (110) and (202) planes of hexagonal Sb (JPCDS No. 35-0732). Besides, XRD patterns of Sb@N-C nanofibers are similar with that of Sb@N-C nanotubes. Figure 2b demonstrates the Raman spectrum of Sb@N-C nanotubes. The strong and broad peaks appear at 1345 and 1587 cm^{-1} can be assigned to the D and G band of the carbon shell. The intensity ratio (I_D/I_G) of Sb@N-C nanotubes is calculated to be about 1.20, indicating the existence of amorphous carbon in the products [31, 32].

The morphologies of Sb@N-C nanofibers and nanotubes are investigated by SEM. Figure 3a, b shows that the Sb@N-C nanofibers are uniform and straight with smooth
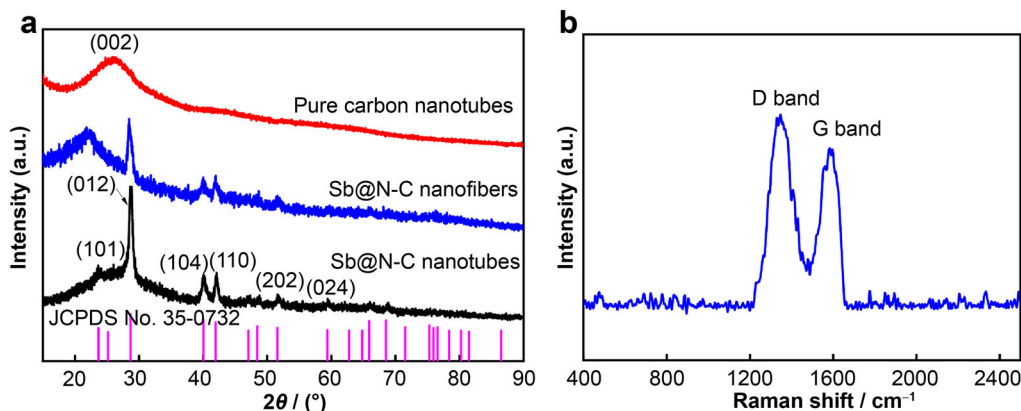

Fig. 2 **a** XRD patterns of pure carbon, Sb@N-C nanofibers and Sb@N-C nanotubes. **b** Raman spectrum of Sb@N-C nanotubes
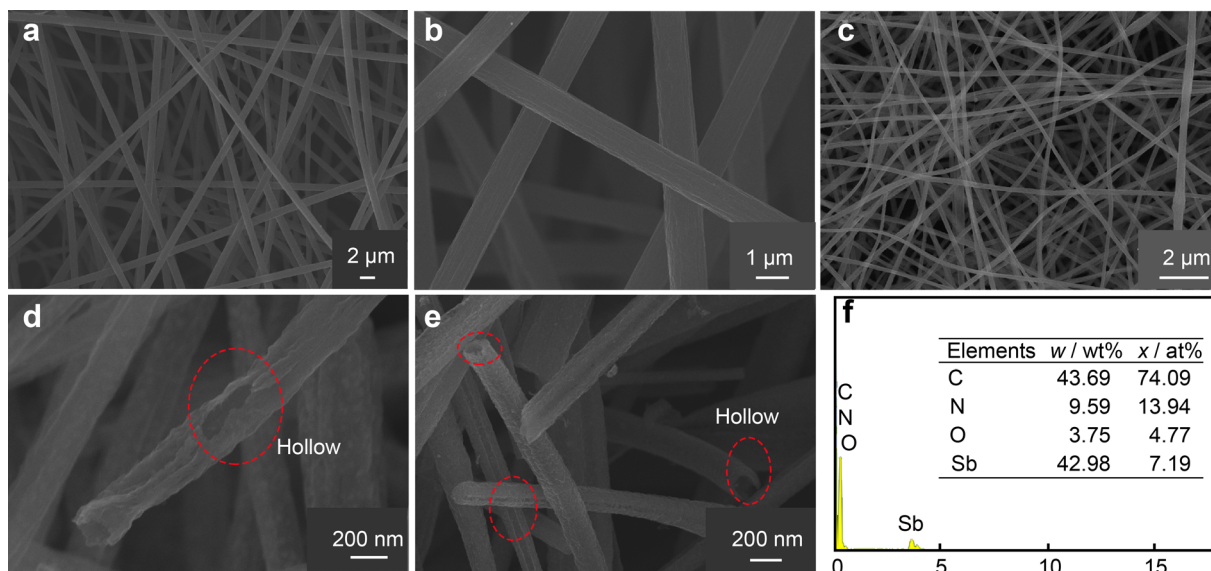
Fig. 3 **a, b** SEM images of Sb@N-C nanofibers, **c–e** SEM images, **f** EDX spectrum of Sb@N-C nanotubes. Inset being specific mass and atomic fraction for each kind of element

surface, and the diameters are about 900 nm. Meanwhile, it can be seen that these nanofibers are solid from the cross section of the Sb@N-C nanofibers in Fig. S2a. The weight percentage of Sb in Sb@N-C nanofibers is 37.03% from the energy-dispersive X-ray spectrometry (EDX) spectrum (Fig. S2b). The morphologies of Sb@N-C nanotubes are different from that of Sb@N-C nanofibers due to the addition of PMMA. As displayed in Fig. 3c–e, plenty of wrinkles appear on the surface of the Sb@N-C nanotubes and the diameter of the nanotubes is reduced to 200–300 nm. Meanwhile, the Sb@N-C nanotubes exhibit a hollow structure and Sb nanoparticles are embedded in the carbon nanotubes. For comparison, pure carbon nanotubes without adding $SbCl_3$ exhibit a hollow porous structure with a diameter about 400 nm (Fig. S3). As displayed in Fig. 3f, the EDX spectrum of Sb@N-C nanotubes reveals the existence of Sb, C, N and O, and the inset illustrates the specific mass and atomic fraction of each kind of element. The weight percentage of Sb, C, N and O in Sb@N-C nanotubes is 42.98%, 43.69%, 9.59% and 3.75%, respectively. Elemental analysis is also conducted to determine the contents of C and N elements, and the result in Table S1 illustrates that the weight percentage of C and N in Sb@N-C nanotubes is 44.92% and 10.73%, which is consistent with the results of EDX.

The morphologies and microstructures of Sb@N-C nanotubes are also investigated by TEM and high-resolution TEM (HRTEM). Figure 4a, b reveals that the Sb@N-C nanotubes have a hollow and porous structure. Sb nanoparticles with a size about 15 nm are embedded in the carbon matrix. The hollow carbon shell can prevent the Sb nanoparticles from volume expansion and aggregation. The

long and hollow porous structure ensures the infiltration of the electrolyte and fast transfer of the electrons/ions. The HRTEM image (Fig. 4c) shows lattice fringes of 0.353, 0.215 and 0.193 nm, which can be indexed to the (101), (110) and (015) planes of Sb. Selected area electron diffraction (SAED) pattern (Fig. 4d) confirms the formation of highly crystalline rhombohedral phase Sb.

As displayed in Fig. 5, XPS is also conducted to further analyze the surface chemical composition of Sb@N-C nanotubes. The survey XPS spectrum (Fig. 5a) illustrates the presence of Sb, C, N and O elements in Sb@N-C nanotubes. As shown in Fig. 5b, two peaks at 538.4 and 528.9 eV can be assigned to Sb $3d_{3/2}$ and Sb $3d_{5/2}$ of Sb nanoparticles, respectively. Additionally, the observed binding energy of O 1s at 530.9 eV in XPS spectrum of Sb 3d may be attributed to surface oxidation of the sample [26]. Three peaks centered at 286.6, 285.6 and 284.8 eV displayed in Fig. 5c can be ascribed to C–O, C=N and C–C bonding configurations, respectively [23]. Figure 5d illustrates the high-resolution of N 1s XPS spectrum, which can be decomposed into three components located at 400.5, 399.9 and 398.3 eV, corresponding to the graphitic N, pyrrolic N and pyridinic N, respectively [33], which confirms the N-doping in Sb@N-C nanotubes.

The electrochemical performances of Sb@N-C nanotubes anode in LIBs are tested by directly using the freestanding Sb@N-C nanotubes as the working electrode. CV curves are measured at a scan rate of 0.1 mV·s^{-1} between 0.01 and 3 V (vs. Li/Li$^+$). As illustrated in Fig. 6a, in the first cathodic sweep, three peaks located at 1.39, 0.83 and 0.54 V can be ascribed to the formation of the solid electrolyte interphase (SEI) and the multistep Li-
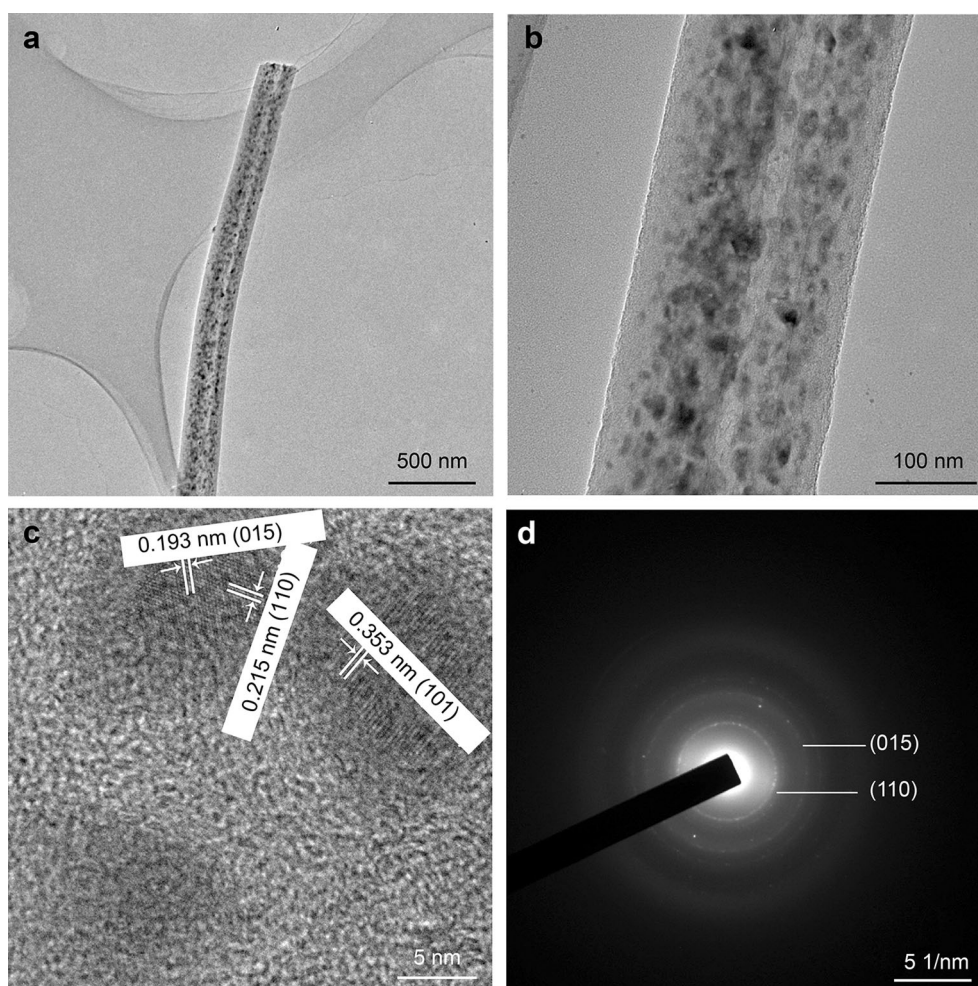
Fig. 4 **a, b** TEM images, **c** HRTEM image, **d** SAED pattern of Sb@N-C nanotubes

Sb alloying reactions [34]. The following anodic peaks centered at 1.39 and 1.15 V are corresponding to the delithiation of Li$_3$Sb [35]. In subsequent cycles, the almost overlapped curves suggest an outstanding cycling reversibility of Sb@N-C nanotubes anode. The galvanostatic discharge–charge (GCD) profiles of Sb@N-C nanotubes for the first, second, third, hundredth, one hundred fiftieth and two hundredth cycles at a current density of 0.1 A·g^{-1} are presented in Fig. 6b. The voltage platforms are consistent with the CV results in Fig. 6a. The initial discharge/charge capacities of Sb@N-C anode are 1033.1 and 756.4 mAh·g^{-1}. The irreversible loss of capacity can be ascribed to the formation of SEI films. The following hundredth, one hundred fiftieth and two hundredth almost overlap, suggesting a good cycling stability of the anode. Figure 6c displays the cycling performance of Sb@N-C nanotubes, Sb@N-C nanofibers and pure carbon nanotubes at a current density of 0.1 A·g^{-1}. The Sb@N-C nanotubes anode can deliver a reversible capacity of 643 mAh·g^{-1} after 250 cycles. The gradual capacity increase during the cycling can be attributed to the activation of the electrode and the reversible formation and decomposition of an organic polymer gel-like film of electrode [36, 37]. However, the pure carbon nanotubes deliver a very low capacity of 148 mAh·g^{-1} after 200 cycles, and the capacity of Sb@N-C nanofibers is sharply decreased to 370 mAh·g^{-1}. Rate properties of Sb@N-C nanotubes are also conducted at different capacities from 0.1 to 10.0 A·g^{-1}. As shown in Fig. 6d, the Sb@N-C nanotubes deliver best rate performances out of three samples. Specifically, Sb@N-C nanotubes show reversible capacities of 695.9, 597.4, 509.5, 431.1, 361, 284.8, 219.6 mAh·g^{-1} at current densities of 0.1, 0.2, 0.5, 1.0, 2.0, 5.0, 10.0 A·g^{-1}, respectively. When the current density returns to 0.1 A·g^{-1}, the capacity recovers to 618 mAh·g^{-1}. In contrast, Sb@N-C nanofibers and pure carbon nanotubes can only deliver 43.5 mAh·g^{-1} and 50.9 mAh·g^{-1} at 10 A·g^{-1}. This result suggests favorable reaction kinetics and excellent reversibility of the Sb@N-C nanotubes electrode.

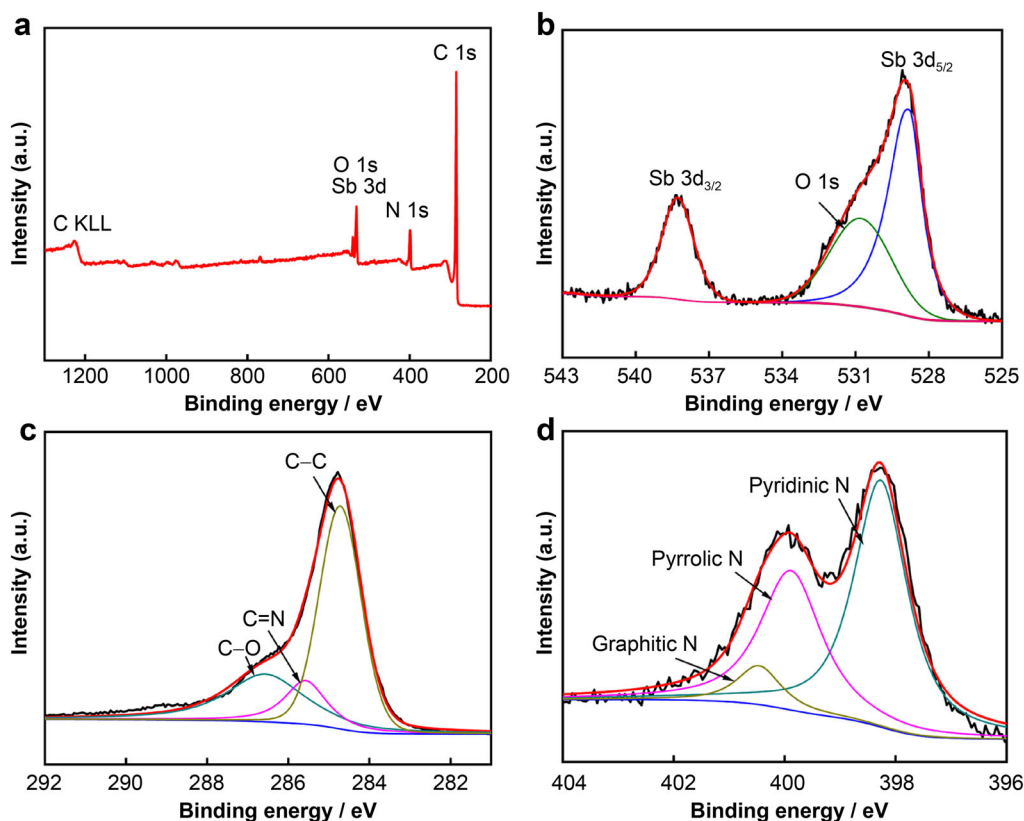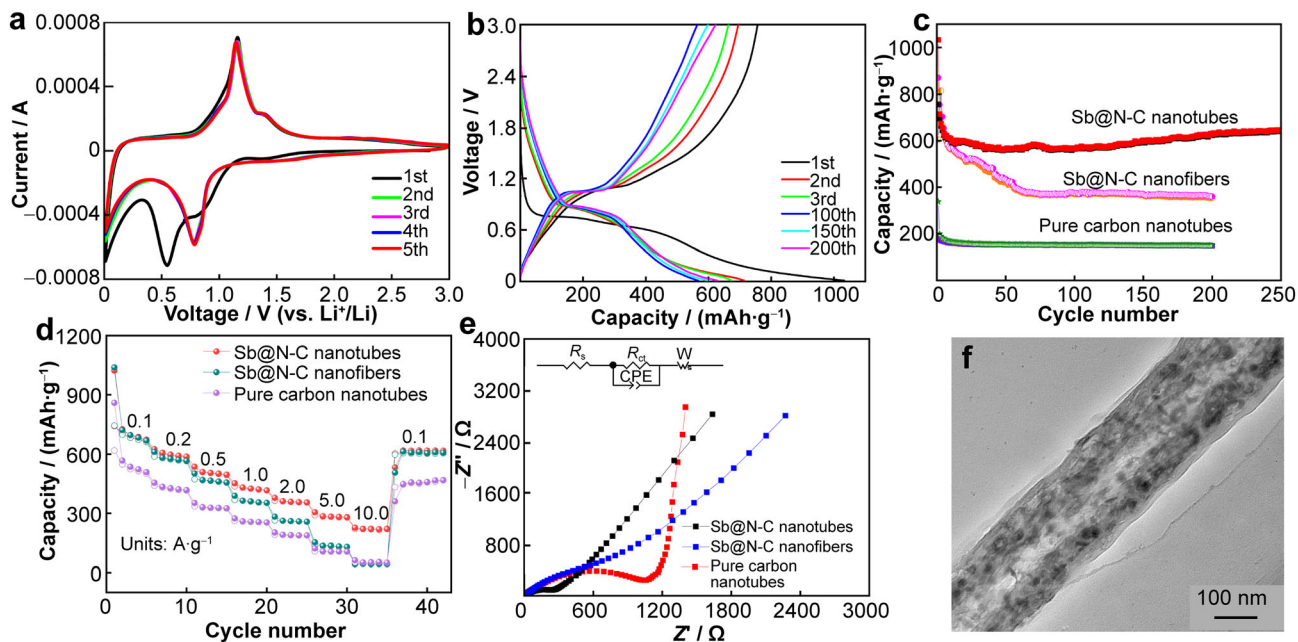Fig. 5 a XPS survey spectrum of Sb@N-C nanotubes and high-resolution spectra of b Sb 3d, c C 1s, and d N 1s

Fig. 6 Electrochemical performances of Sb@N-C nanotubes in LIBs: a CV curves at a scan rate of 0.1 mV·s⁻¹; b GCD profiles at a current density of 0.1 A·g⁻¹; c cycling performance of Sb@N-C nanotubes, Sb@N-C nanofibers and pure carbon nanotubes at a current density of 0.1 A·g⁻¹; d rate performance of Sb@N-C nanotubes, Sb@N-C nanofibers, and pure carbon nanotubes at different current densities; e Nyquist plots of Sb@N-C nanotubes, Sb@N-C nanofibers and pure carbon nanotubes, inset being equivalent circuit model; f TEM image of Sb@N-C nanotubes after 250 cycles
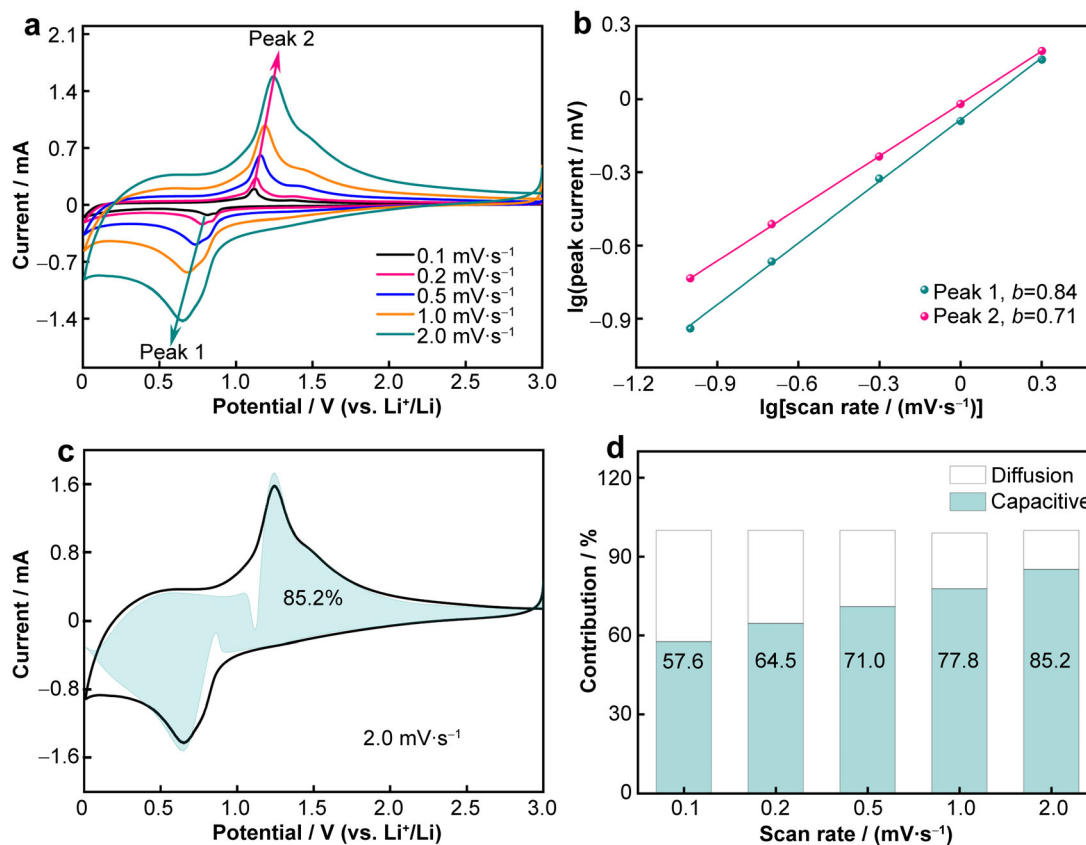
Fig. 7 **a** CV curves of Sb@N-C nanotubes at increasing scan rates from 0.1 to 2.0 mV·s⁻¹; **b** relationships between lg$i$ versus lg$v$; **c** capacitive contribution at a scan rate of 2.0 mV·s⁻¹; **d** capacitive contribution of Sb@N-C nanotubes at different scan rates

To explore the enhanced electrochemical property of Sb@N-C nanotubes, EIS measurements of Sb@N-C nanotubes, Sb@N-C nanofibers and pure carbon nanotubes are conducted. As shown in Fig. 6e, the semicircle at high-frequency region represents charge transfer resistance (R_{ct}). And the slop line at low-frequency region represents Warburg impedance (R_w) for transportation of lithium ions. The equivalent circuit model fitting with plots is shown in inset of Fig. 6e. The ohmic resistance (R_s) is relevant to the chemical composition of the electrolyte. The constant phase angle element (CPE) is a physical quantity used to describe the deviation of the parameters of the capacitance. The corresponding fitted results are displayed in Table S2. It can be seen that R_{ct} of Sb@N-C nanotubes (252.6 Ω) is smaller than that of Sb@N-C nanofibers (735.8 Ω) and pure carbon nanotubes (1127.0 Ω), which ensuring that Sb@N-C nanotubes have accelerated electronic transportation and fast Li⁺ storage kinetics. Furthermore, TEM image of Sb@N-C nanotubes after 250 cycles is displayed in Fig. 6f. The morphologies of the electrode are basically retained, and the void of nanotubes can be clearly observed from TEM image, which indicates that the enough space

can accommodate volume expansion and agglomeration of Sb nanoparticles, ensuring outstanding structural stability of Sb@N-C nanotubes.

To further evaluate the electrochemical kinetics, CV curves at increasing scan rates from 0.1 to 2.0 mV·s⁻¹ are measured. As shown in Fig. 7a, all the CV curves display similar shapes except slight polarization. The relationship between peak current (i) and sweep rate (v) obeys the following equations [38]:

$$i = av^b \tag{1}$$

$$\lg i = b\lg v + \lg a \tag{2}$$

where a and b are appropriate values. Generally, the b value of 0.5 denotes a diffusion-controlled behavior, and the b-value of 1.0 indicates a capacitive-controlled process [39]. As displayed in Fig. 7b, the b values for anodic peak (Peak 1) and cathodic peak (Peak 2) are 0.84 and 0.71, respectively, indicating lithium ion storage kinetics is capacitive-dominated. Furthermore, the capacitive contribution can be further quantified by the following equation:
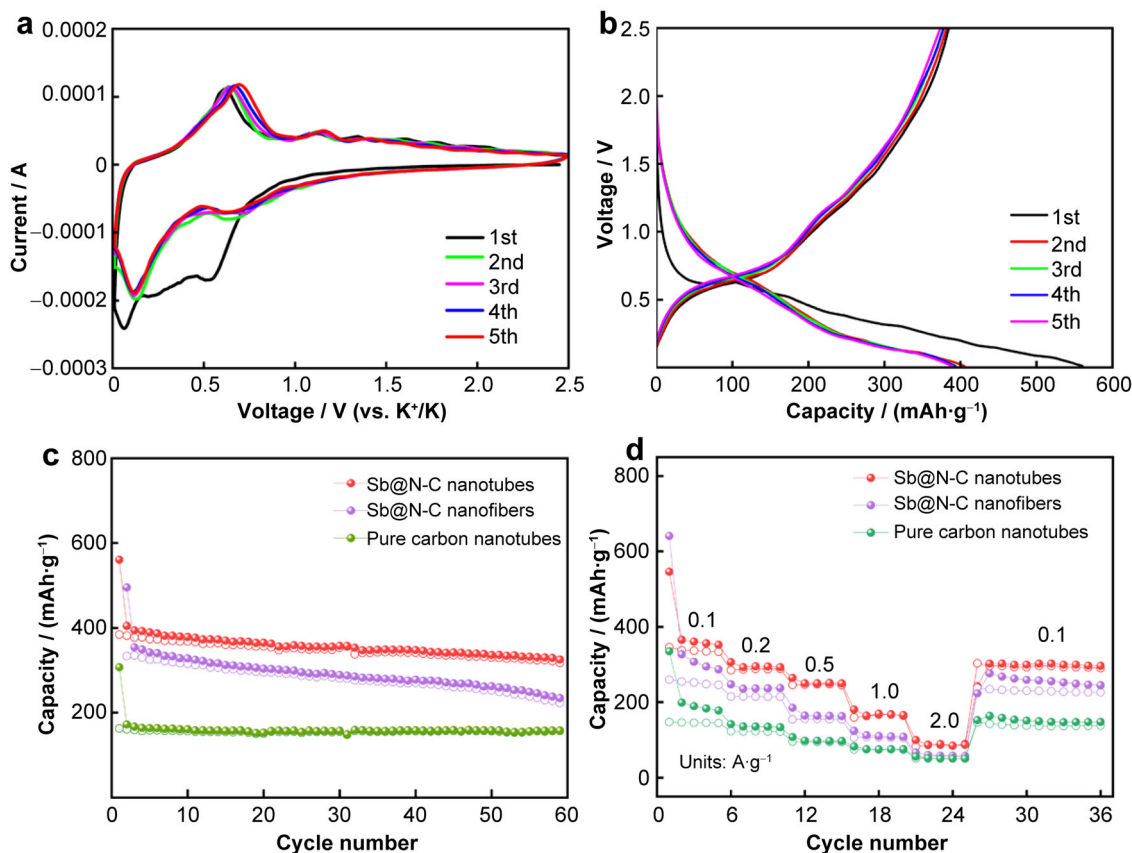
Fig. 8 Electrochemical performances of Sb@N-C nanotubes in PIBs. **a** CV curves of Sb@N-C nanotubes at a scan rate of 0.1 mV·s^{-1}; **b** GCD profiles Sb@N-C nanotubes at a current density of 0.1 A·g^{-1}; **c** cycling performance of Sb@N-C nanotubes, Sb@N-C nanofibers, and pure carbon nanotubes at a current density of 0.1 A·g^{-1}; **d** rate performance of Sb@N-C nanotubes, Sb@N-C nanofibers, and pure carbon nanotubes at different current densities

$$i = k_1 v + k_2 v^{1/2} \qquad (3)$$

where $k_1 v$ and $k_2 v^{1/2}$ stand for the capacitive- and diffusion-controlled contributions, respectively [40]. Figure 7c shows that capacitive contributions (shaded area) in the total charge storage at 2.0 mV·s^{-1} is 85.2%. And the ratio of capacitive contribution increases with increased scan rates (Fig. 7d), which further confirms that lithium ion storage behavior is dominated by capacitive-controlled process. The high portion of capacitive contribution can be attributed to porous hollow structure of Sb@N-C nanotubes, which is beneficial to the electrode reaction, leading to excellent rate performance.

The potassium storage performances of Sb@N-C nanotubes anode were first evaluated by CV in a voltage window ranging from 0.01 to 2.5 V (vs. K/K$^+$) at a scan rate of 0.1 mV·s^{-1} (Fig. 8a). The cathodic peak of the first cycle located at 0.54 V is corresponding to the stepwise of formation of K$_x$Sb alloy and the formation of SEI films. Another reaction peak centered at about 0.07 V can be attributed to both K ions insertion in carbon and the step formation of K$_5$Sb$_4$ and K$_3$Sb alloys [21]. In the following

anodic scan, a distinct peak is located at 0.7 V and a minor peak at 1.16 V, which can be ascribed to the multi-step reaction of K$^+$ deintercalated from K$_x$Sb [41]. The subsequent curves after the second scan almost overlap, suggesting an outstanding reversibility and stability of Sb@N-C nanotubes in PIBs.

Figure 8b demonstrates GCD profiles of Sb@N-C nanotubes from the first to fifth cycles. It can be seen that the sloping plateaus are consistent with CV results. The first discharge and charge capacities are 560.6 mAh·g^{-1} and 384.6 mAh g^{-1}, respectively, with initial Coulombic efficiency of 68.6%. For the Sb@N-C nanofibers, the GCD profiles are similar with that of Sb@N-C nanotubes, while the first discharge and charge capacities are 495.1 and 333.9 mAh·g^{-1}, respectively (Fig. S4).

The cycling performances of Sb@N-C nanotubes, pure carbon nanotubes and Sb@N-C nanofibers at a current density of 0.1 A·g^{-1} in PIBs are illustrated in Fig. 8c. The Sb@N-C nanotubes anode exhibits a stability cycling performance with a capacity of 325.4 mAh·g^{-1} after 60 cycles. In contrast, the pure carbon nanotubes and Sb@N-C nanofibers display a lower capacity of 157.8 and

234.4 mAh·g^{-1} after 60 cycles, respectively. Likewise, the Sb@N-C nanotubes display excellent rate performance compared with other two materials in PIBs (Fig. 8d). The Sb@N–C nanotubes deliver reversible capacities of 360.7, 294.5, 251.1, 169.2 and 88.5 mAh·g^{-1} at current densities of 0.1, 0.2, 0.5, 1.0 and 2.0 A·g^{-1}, respectively. When the current density returns to 0.1 A·g^{-1}, the capacity recovers to 315.3 mAh·g^{-1}, suggesting a stable structure of the electrode during the intercalation and deintercalation of K ions. The remarkable cycling and rate performances of Sb@N-C nanotubes are attributed to the fast transport of K ions and electrons in 3D connected networks. In addition, the hollow and porous carbon shell can buffer the volume expansion during the charging and discharging process.

Electrochemical properties comparison of the as-prepared Sb@N-C nanotubes with reported Sb-based anodes in LIBs and PIBs are illustrated in Table S3. It can be seen that Sb@N-C nanotubes exhibit superior performances, which can be attributed the unique structure of the Sb@N-C nanotubes. Sb nanoparticles are evenly distributed in the hollow porous N-doped carbon nanotubes, which can not only provide quick transfer channels for ions and electrons, but also provide extra space to buffer the volume expansion of Sb nanoparticles. Therefore, an improved electrochemical performance can be obtained.

4 Conclusion

In conclusion, a universal binder-free anode for alkali metal ion batteries based on freestanding Sb@N-C nanotubes are fabricated by a typical electrospinning and subsequently annealing process with PMMA as pore former. It exhibits a remarkable cycling performance with reversible capacities of 643 mAh·g^{-1} after 250 cycles in LIBs and 325.4 mAh·g^{-1} after 60 cycles in PIBs, respectively. The enhanced electrochemical performances can be attributed to the hollow porous structure of the electrode, in which N-doped carbon network can enhance the transport of ions and electrons, and hollow porous nanotubes can provide space to buffer the volume expansion of Sb nanoparticles, ensuring structural stability. This work paves a pathway to design universal structure of anode materials for flexible alkali metal ion batteries.

Declarations

Conflict of interests The authors declare that they have no conflict of interest.

References

[1] Hu Y, Sun X. Flexible rechargeable lithium ion batteries: advances and challenges in materials and process technologies. J Mater Chem A. 2014;2(28):10712. https://doi.org/10.1039/C4TA00716F.

[2] Lin XP, Xue DY, Zhao LZ, Zong FY, Duan XC, Pan X, Zhang JM, Li QH. In-situ growth of 1T/2H-MoS$_2$ on carbon fiber cloth and the modification of SnS$_2$ nanoparticles: a three-dimensional heterostructure for highperformance flexible lithium-ion batteries. Chem Eng J. 2019;356(15):483. https://doi.org/10.1016/j.cej.2018.08.208.

[3] Hu XL, Zhang W, Liu XX, Mei YN, Huang YH. Nanostructured Mo-based electrode materials for electrochemical energy storage. Chem Soc Rev. 2015;44(8):2376. https://doi.org/10.1039/C4CS00350K.

[4] Xue FF, Li YY, Liu C, Zhang ZG, Lin J, Hao JY, Li QH. Engineering flexible carbon nanofiber concatenated MOF-derived hollow octahedral CoFe$_2$O$_4$ as an anode material for enhanced lithium storage. Inorg Chem Front. 2021;8(13):3363. https://doi.org/10.1039/D1QI00414J.

[5] Zhang Y, Chen PH, Gao X, Wang B, Liu H, Wu H, Liu HK, Dou SX. Nitrogen-doped graphene ribbon assembled core-sheath MnO@graphene scrolls as hierarchically ordered 3D porous electrodes for fast and durable lithium storage. Adv Funct Mater. 2016;26(43):7754. https://doi.org/10.1002/adfm.201603716.

[6] Zhao ZJ, Chao YG, Wang F, Dai JY, Qin YF, Bao XB, Yang Y, Guo SJ. Intimately coupled WS$_2$ nanosheets in hierarchical hollow carbon nanospheres as the high-performance anode material for lithium-ion storage. Rare Met. 2022;41(4):1245. https://doi.org/10.1007/s12598-021-01850-w.

[7] Zhao J, Li CL, Chen G, Ji F, Shen YY, Peng J, Wang WH. Rational design of Sn$_4$P$_3$/Ti$_3$C$_2$T$_x$ composite anode with enhanced performance for potassium-ion battery. Rare Met. 2022. https://doi.org/10.1007/s12598-021-01934-7.

[8] Yang WX, Zhou JX, Wang S, Zhang WY, Wang ZC, Lv F, Wang K, Sun Q, Guo SJ. Freestanding film made by necklace-like N-doped hollow carbon with hierarchical pores for high-performance potassium-ion storage. Energy Environ Sci. 2019;12(5):1605. https://doi.org/10.1039/C9EE00536F.

[9] Lin HZ, Li ML, Yang X, Yu DY, Zeng Y, Wang CZ, Chen G, Du F. Nanosheets assembled CuSe crystal pillar as a stable and high-power anode for sodium-ion and potassium-ion batteries. Adv Energy Mater. 2019;9(20):1900323. https://doi.org/10.1002/aenm.201900323.

[10] Xue FF, Lin XP, Li YY, Zhang ZG, Lin J, Li QH. Electrospun of CoSn nanoboxes@carbon nanotubes as free-standing anodes for high-performance lithium-/potassium-ion batteries. Appl Surf Sci. 2021;565(1):150599. https://doi.org/10.1016/j.apsusc.2021.150599.

[11] Liao JY, Chen CL, Hu Q, Du YC, He YN, Xu YF, Zhang ZZ, Zhou XS. A low-strain phosphate cathode for high-rate and ultralong cycle life potassium-ion batteries. Angew Chem Int Ed. 2021;60(48):25575. https://doi.org/10.1002/anie.202112183.

[12] He YN, Xu YF, Zhang M, Xu JZ, Chen BB, Zhang YX, Bao JC, Zhou XS. Confining ultrafine SnS nanoparticles in hollow multichannel carbon nanofibers for boosting potassium storage properties. Sci Bull. 2022;67(2):151. https://doi.org/10.1016/j.scib.2021.09.020.

[13] He XD, Liu ZH, Liao JY, Ding X, Hu Q, Xiao LN, Wang S, Chen CH. A three-dimensional macroporous antimony@carbon composite as a high-performance anode material for potassium-ion batteries. J Mater Chem A. 2019;7(16):9629. https://doi.org/10.1039/C9TA01968E.

[14] Zheng J, Yang Y, Fan XL, Ji GB, Ji X, Wang HY, Hou S, Zachariah MR, Wang CS. Extremely stable antimony–carbon composite anodes for potassium-ion batteries. Energy Environ Sci. 2019;12(2):615. https://doi.org/10.1039/C8EE02836B.

[15] Mao ML, Cui CY, Wu MG, Zhang M, Gao T, Fan XL, Chen J, Wang TH, Ma JM, Wang CS. Flexible ReS₂ nanosheets/N-doped carbon nanofibers-based paper as a universal anode for alkali (Li, Na, K) ion battery. Nano Energy. 2018;45:346. https://doi.org/10.1016/j.nanoen.2018.01.001.

[16] Zhao WX, Zou L, Ma XQ, Zhang WL, Li YD, Wang GZ, Zhang P, Xia LP. Ultrafine Sb nanoparticles embedded in nitrogen-doped carbon nanofibers as ultralong cycle durability and high-rate anode materials for reversible sodium storage. Electrochim Acta. 2019;300:396. https://doi.org/10.1016/j.electacta.2019.01.138.

[17] Xu X, Si L, Zhou XS, Tu FZ, Zhu XS, Bao JC. Chemical bonding between antimony and ionic liquid-derived nitrogen-doped carbon for sodium-ion battery anode. J Power Sources. 2017;349:37. https://doi.org/10.1016/j.jpowsour.2017.03.026.

[18] Li HX, Wang JW, Jiao LF, Tao ZL, Liang J. Spherical nano-SnSb/C composite as a high-performance anode material for sodium ion batteries. Acta Phys Chim Sin. 2020;36(5):1904017. https://doi.org/10.3866/PKU.WHXB201904017.

[19] Song JH, Yan PF, Luo LL, Qi XG, Rong XH, Zheng JM, Xiao BW, Feng S, Wang CM, Hu YS, Lin YH, Sprenkle VL, Li XL. Yolk-shell structured Sb@C anodes for high energy Na-ion batteries. Nano Energy. 2017;40:504. https://doi.org/10.1016/j.nanoen.2017.08.051.

[20] Liang LY, Xu Y, Wen LY, Li YL, Zhou M, Wang CL, Zhao HP, Kaiser U, Lei Y. Hierarchical Sb-Ni nanoarrays as robust binder-free anodes for high-performance sodium-ion half and full cells. Nano Res. 2017;10:3189. https://doi.org/10.1007/s12274-017-1536-0.

[21] Yi Z, Han QG, Zan P, Wu YM, Cheng Y, Wang LM. Sb nanoparticles encapsulated into porous carbon matrixes for high-performance lithium-ion battery anodes. J Power Sources. 2016. https://doi.org/10.1016/j.jpowsour.2016.09.027.

[22] Luo W, Lorger S, Wang B, Bommier C, Ji XL. Facile synthesis of one-dimensional peapod-like Sb@C submicron-structures. Chem Commun. 2014;50(41):5435. https://doi.org/10.1039/C4CC01326C.

[23] Li QH, Zhang W, Peng J, Zhang W, Liang ZX, Wu JW, Feng JJ, Li HX, Huang SM. Metal-organic framework derived ultrafine Sb@porous carbon octahedron via in situ substitution for high-performance sodiumIon batteries. ACS Nano. 2021;15(9):15104. https://doi.org/10.1021/acsnano.1c05458.

[24] Hou HS, Jing MJ, Yang YC, Zhang Y, Zhu YR, Song WX, Yang XM, Ji XB. Sb porous hollow microspheres as advanced anode materials for sodium-ion batteries. J Mater Chem A. 2015;3(6):2971. https://doi.org/10.1039/C4TA06476C.

[25] Mao ML, Yan FL, Cui CY, Ma JM, Zhang M, Wang TH, Wang CS. Pipe-wire TiO₂-Sn@carbon nanofibers paper anodes for lithium and sodium ion batteries. Nano Lett. 2017;17(6):3830. https://doi.org/10.1021/acs.nanolett.7b01152.

[26] Huang HW, Wang JW, Yang XF, Hu RZ, Liu JL, Zhang L, Zhu M. Unveiling the advances of nanostructure design for alloy-type potassium-ion battery anodes via in situ TEM. Angew Chem Int Ed. 2020;59(34):2. https://doi.org/10.1002/anie.202004193.

[27] Yu Y, Gu L, Zhu CB, van Aken PA, Maier J. Tin nanoparticles encapsulated in porous multichannel carbon microtubues preparation by single-nozzle electrospinning and application as anode material for high-performance Li-based batteries. J Am Chem Soc. 2009;131(44):15984. https://doi.org/10.1021/ja906261c.

[28] Bazilevsky AV, Yarin AL, Megaridis CM. Co-electrospinning of core-shell fibers using a single-nozzle technique. Langmuir. 2007;23(5):2311. https://doi.org/10.1021/la063194q.

[29] Kim C, Jeong YI, Ngoc BTN, Yang KS, Kojima M, Kim YA, Endo M, Lee JW. Synthesis and characterization of porous carbon nanofibers with hollow cores through the thermal treatment of electrospun copolmeric nanofiber webs. Small. 2007;3(1):91. https://doi.org/10.1002/smll.200600243.

[30] Hong CK, Yang KS, Oh SH, Ahn JH, Cho BH, Nah CC. Effect of blend composition on the morphology development of electrospun fibres based on PAN/PMMA blends. Polym Int. 2008;57(12):1357. https://doi.org/10.1002/pi.2481.

[31] Qin J, He CN, Zhao NQ, Wang ZY, Shi CS, Liu EZ, Li JJ. Graphene networks anchored with Sn@graphene as lithium ion battery anode. ACS Nano. 2014;8(2):1728. https://doi.org/10.1021/nn406105n.

[32] Li XF, Dhanabalan A, Gu L, Wang CL. Three-dimensional porous core-shell Sn@carbon composite anodes for high-performance lithium-ion battery applications. Adv Energy Mater. 2012;2(2):238. https://doi.org/10.1002/aenm.201100380.

[33] Chen RP, Xue XL, Lu JY, Chen T, Hu Y, Ma LB, Zhu GY, Jin Z. The dealloying-lithiation/delithiation-realloying mechanism of a breithauptite (NiSb) nanocrystal embedded nanofabric anode for flexible Li-ion batteries. Nanoscale. 2019;11(18):8803. https://doi.org/10.1039/C9NR00159J.

[34] Zhang N, Liu YC, Lu YY, Han XP, Cheng FY, Chen J. Spherical nano-Sb@C composite as a high-rate and ultra-stable anode material for sodium-ion batteries. Nano Res. 2015;8:3384. https://doi.org/10.1007/s12274-015-0838-3.

[35] Yang QQ, Zhou J, Zhang GQ, Guo C, Li M, Zhu YC, Qian YT. Sb nanoparticles uniformly dispersed in 1-D N-doped porous carbon as anodes for Li-ion and Na-ion batteries. J Mater Chem A. 2017;5(24):12144. https://doi.org/10.1039/C7TА0F.

[36] Yu H, Fan HS, Yadian B, Tan HT, Liu WL, Hng HH, Huang YZ, Yan QY. General approach for MOF-derived porous spinel AFe₂O₄ hollow structures and their superior lithium storage properties. ACS Appl Mater Interfaces. 2015;7(48):26751. https://doi.org/10.1021/acsami.5b08741.

[37] Hu YY, Liu ZG, Nam KW, Borkiewicz OJ, Cheng J, Hua X, Dunstan MT, Yu XQ, Wiaderek KM, Du LS, Chapman KW, Chupas PJ, Yang XQ, Grey CP. Origin of additional capacities in metal oxide lithium-ion battery electrodes. Nat Mater. 2013;12:1130. https://doi.org/10.1038/nmat3784.

[38] Yang T, Liu JW, Yang DX, Mao QN, Zhong JS, Yuan YJ, Li XY, Zheng X, Ji ZG, Liu H, Wang GX, Zheng RK. Bi₂Se₃@C rod-like architecture with outstanding electrochemical properties in lithium/potassium-ion batteries. ACS Appl Energy Mater. 2020;3(11):11073. https://doi.org/10.1021/acsaem.0c02056.

[39] Xu LH, Chen XC, Guo WT, Zeng LX, Yang T, Xiong PX, Chen QH, Zhang JM, Wei MD, Qian QR. Co-construction of sulfur vacancies and carbon confinement in V₅S₈/ CNFs to induce an ultra-stable performance for half/full sodium-ion and potassium-ion batteries. Nanoscale. 2021;13(9):5033. https://doi.org/10.1039/D0NR08788B.

[40] Zhang ZG, Lin J, Hao JY, Xue FF, Gu YF, Zhu ZC, Li QH. Exploration of fast ion diffusion kinetics in graphene nanoscrolls encapsulated CoSe₂ as advanced anode for high-rate sodium-ion batteries. Carbon. 2021;181(30):69. https://doi.org/10.1016/j.carbon.2021.04.095.

[41] Wang H, Wu X, Qi XJ, Zhao W, Ju ZC. Sb nanoparticles encapsulated in 3D porous carbon as anode material for lithium-ion and potassium-ion batteries. Mater Res Bull. 2018;103:32. https://doi.org/10.1016/j.materresbull.2018.03.018.